Research Article Vol. 31, No. 26 / 18 Dec 2023 / Optics Express 43950
Optics EXPRESS

Day and night continuous high-resolution shallow-water depth detection with single-photon underwater lidar

MINGJIA SHANGGUAN,[1,*] ZHENWU WENG,[1] ZAIFA LIN,[1] ZHONGPING LEE,[1] MINGYU SHANGGUAN,[2] ZHIFENG YANG,[1] JIAXIN SUN,[1] TENGFEI WU,[3] YU ZHANG,[1] AND CEHNGLU WEN[4]

[1]*State Key Laboratory of Marine Environmental Science, College of Ocean and Earth Sciences, Xiamen University, Xiamen 361102, China*
[2]*Fuzhou Dayu Electronic Technology Co., Ltd, Fujian 350021, China*
[3]*Science and Technology on Metrology and Calibration Laboratory, Changcheng Institute of Metrology and Measurement, Aviation Industry Corporation of China, Beijing 100095, China*
[4]*Fujian Key Laboratory of Sensing and Computing for Smart Cities, School of Informatics, Xiamen University, Xiamen, China*
[*]*mingjia@xmu.edu.cn*

Abstract: Single-photon lidar has emerged as a strong technology for bathymetric measurements. However, its heightened sensitivity additionally makes it susceptible to solar radiation noise, particularly in the green light wavelength where solar radiation is strong, posing challenges for its daytime operation. To address this issue, a single-photon underwater lidar system is proposed and demonstrated. This scheme has these features. 1) Underwater applications not only mitigate the impact of the air-water interface on laser transmission but also significantly attenuate solar radiation reaching the lidar due to the absorption and scattering properties of water. 2) The telescope is designed with a small aperture and narrow field of view to significantly suppress solar radiation. 3) A combination of a narrowband laser and narrowband filter technique is effectively employed to minimize residual solar radiation, thus enabling continuous bathymetric observation capabilities during both day and night. 4) After acquiring the backscattered signal from the bottom, a water depth extraction algorithm utilizing bi-Gaussian fitting is proposed. To demonstrate the robustness of the lidar and the effectiveness of the algorithm, the underwater single-photon lidar system is deployed on a ship to conduct cruise surveys of two bays in the nearshore area, as well as a full-day stationary observation experiment. The lidar measurements are highly consistent with the synchronized sonar observations. The full-day stationary observation experiment showcased its capability to deliver continuous measurements throughout the day and night. These results demonstrate the potential of the system in various applications, including high-precision underwater terrain mapping, obstacle avoidance for underwater platforms, and underwater target imaging.

1. Introduction

Accurate measurement and monitoring of underwater topography and geomorphology are essential for safe navigation, scientific research, and management of marine ecosystems. Bathymetric lidar is an important tool for measuring water depth with high depth resolution. Depending on the water clarity, the lidar system is capable of measuring water depths ranging from 1.5 m to 60 m, which is ~ three times the Secchi depths (SD) [1]. Furthermore, due to the ability of lidar to penetrate the air-water interface, it possesses the flexibility for deployment and has been applied on various platforms such as ships, unmanned aerial vehicles (UAVs), aircraft, and satellites [2].

#505865 https://doi.org/10.1364/OE.505865
Journal © 2023 Received 13 Sep 2023; revised 23 Nov 2023; accepted 29 Nov 2023; published 12 Dec 2023

Optics EXPRESS

Bathymetric lidar technology can be divided into two main types: full-waveform lidar and single-photon lidar [3]. These two types of lidar systems typically utilize a blue-green pulse laser, such as a 532 nm green laser, or a combination of an infrared 1064 nm laser and its second-harmonic 532 nm laser. By incorporating an additional pulsed infrared laser, more accurate information about the water surface can be obtained [4]. In the case of full-waveform lidar, depth information is derived by analyzing the complete waveform. Several waveform processing algorithms have been proposed for bathymetry lidar, which can be divided into three groups: return detection, mathematical approximation, and deconvolution [5]. With the maturation of full-waveform bathymetric lidar technology, numerous airborne bathymetric lidars utilizing full waveform techniques have been developed since 1973 [6]. Examples of these systems include the NASA Airborne Oceanographic lidar, the Canadian Larsen 500, the Australian WRELADS, the Swedish FLASH, Royal Australian Navy's Laser Airborne Depth Sounder, the U.S. Army Corps of Engineers' Scanning Hydrographic Operational Airborne Laser Survey, and the Swedish Maritime Administration's HawkEye, among others [7].

The advantages of full-waveform bathymetry lidar include providing sharper and more precise mapping of topography compared to single-photon counting technology [3]. Additionally, it enables the secondary analysis of full-waveform data, including parameters such as the peak amplitude, pulse width, area, skewness, etc., allowing for the classification of coral reefs [8] and seafloor [9–11]. To improve signal-to-noise ratio (SNR), full-waveform lidar technology typically utilizes laser with high-pulse-energy. However, this can result in increased power consumption and larger system size. To address these limitations and enable deployment on small platforms like UAVs, compact UAV-borne full-waveform bathymetry lidars have been developed and even commercialized. Examples include RIEGL VQ-840-G [12], ASTRALiTe edge [13], and Fugro RAMMS [14]. These systems can achieve detection depths of approximately twice the transparency of the water body [12].

Alternatively, single-photon lidar technology can achieve long-range detection using micro-pulse laser and small aperture telescope by enhancing detector sensitivity to the single-photon level [15–20]. Therefore, NASA's Ice, Cloud, and land Elevation Satellite-2 (ICESat-2) adopted a photon-counting instrument design and has demonstrated seafloor detection at depths of up to ~ 40 m, with root mean square error (RMSE) values between 0.26 m and 0.61 m [21,22]. Furthermore, the low energy requirements of single-photon lidar also allow micro-joule laser to be split into 100 beamlets, enabling reliable identification and removal of noise events [23]. This technology enables the development of compact and highly integrated bathymetric lidar systems [24–26].

However, the high sensitivity of single-photon lidar makes it susceptible to background noises, particularly solar radiation noise. This is particularly challenging during daylight operation as the blue-green wavelength band commonly used in bathymetry lidars overlaps with the strongest solar radiation background [26]. To overcome this limitation, this work proposes and demonstrates a single-photon underwater lidar (SPUL) that can continuous operate day and night. Firstly, underwater lidar overcomes the challenges posed by sea-air interface interference faced by aerial lidar systems, especially under poor sea conditions [27]. On one hand, utilizing this feature, underwater lidar can be utilized for the calibration of oceanic lidar systems operating above the water surface, including airborne or satellite lidar. On the other hand, by leveraging its high-resolution characteristics, and the ability to profile the vertical distribution of particles and dissolved matter [19,20], it complements sonar technology for underwater environmental surveys. Simultaneously, this miniaturized single-photon lidar can be deployed on unmanned surface vessels (USVs) for underwater terrain and geomorphology mapping, as well as on underwater platforms such as Autonomous Underwater Vehicles (AUVs) or Remotely Operated Vehicles (ROVs). Therefore, it enables accurate depth measurements in shallow waters and functions as an obstacle avoidance system for underwater platforms [28]. Secondly, solar radiation is attenuated

Optics EXPRESS

as it travels from the water surface to the location of the underwater lidar due to the absorption and scattering properties of water, with greater attenuation observed with lidar deployment over deeper water [26]. Therefore, once the lidar is deployed underwater, whether it is full-waveform lidar or single-photon lidar, it benefits from the reduced solar radiation, resulting in an enhanced signal-to-noise ratio (SNR) for detection. Thirdly, the telescope is designed with a small aperture (4.8 mm) and narrow field of view (9.6 mrad) to significantly suppress solar radiation. Finally, a combination of a narrowband laser and narrowband filter technique is effectively employed to minimize residual solar radiation, thus enabling continuous bathymetric observation capabilities with single-photon lidar during both day and night.

In terms of algorithms, single-photon lidars differ from full-waveform lidars, as they determine water depth by statistically analyzing the probability distribution of photons rather than analyzing waveform data [29–31]. Although this statistical approach enables single-photon lidars to achieve better performance on area coverage with only a small number of photons, it comes at the cost of sacrificing detailed waveform information. In this work, photon-reconstructed waveform is achieved through the cumulative histograms. To achieve this, a hardware design incorporating a high pulse repetition rate (1 MHz) green laser and a high-sampling-rate time-to-digital converter (TDC) has been implemented. Regarding the algorithm for depth retrieval, a nonlinear least square fitting approach using bi-Gaussian function is employed. Simulation analysis has shown that this method can improve the accuracy of bottom depth inversion to the level of cm.

The article is organized as follows: Firstly, the SPUL is introduced, including an exposition of the techniques used to suppress solar radiation. Secondly, the algorithm used to retrieve bottom depth is presented, and the accuracy of the inversion is analyzed. Following this, two field experiments are described, consisting of two cruise surveys and a stationary observation experiment lasting 24 hours. Finally, the conclusion is presented.

2. Single-photon underwater lidar system

Figure 1(b) illustrates the schematic diagram of the setup for the SPUL, which comprises three subsystems: a 532 nm pulsed laser, a transceiver, and a data acquisition system. Taking into consideration that green lasers perform better than blue lasers in most coastal waters [32], and considering the commercial availability, robustness, and suitability for operation in harsh environments of the 532 nm laser, the laser wavelength selected for the SPUL is 532 nm. The laser system utilizes a compact fiber-based picosecond laser employing a master oscillator power amplifier (MOPA) architecture. The seed laser, operating at 1064 nm, is a single-mode single-frequency pulsed laser. It undergoes amplification via a single-mode ytterbium-doped fiber amplifier (SM-YDFA) and two-stage high-power ytterbium-doped fiber amplifiers (HP-YDFAs). Subsequently, the laser passes through a lithium borate (LBO) crystal for second harmonic generation, resulting in output at 532 nm with an average power output of up to 100 mW with a beam divergence of 0.5 mrad. The output laser pulse has a full width at half maximum (FWHM) of 501 ps, and the spectral linewidth is 0.04 nm. The pulse repetition rate is 1 MHz, with a pulse energy of 100 nJ.

To achieve a miniaturized and robust structure, a fiber-connected configuration is specifically designed for the single-photon lidar system. The backscattered signal is collected using a collimator (Thorlabs, F220APC-532) with a narrowband filter placed in front of it. The half-inch filter has a bandwidth of 0.08 nm, and its center wavelength aligns with the laser wavelength. The 532 nm backscattered signal is coupled into a multimode fiber (MMF) with a core diameter of 105 μm and a numerical aperture (NA) of 0.22 through the collimator with a 10.9 mm focal length. This results in a narrow field of view of ~ 9.6 mrad. The combination of the small collimator and narrow FOV contributes to the suppression of background noise. The distance between the transmitted laser and the received collimator is ~ 10 mm. Due to the close proximity of the transmitter and receiver, as well as the multiple scattering effects when laser propagates

Optics EXPRESS

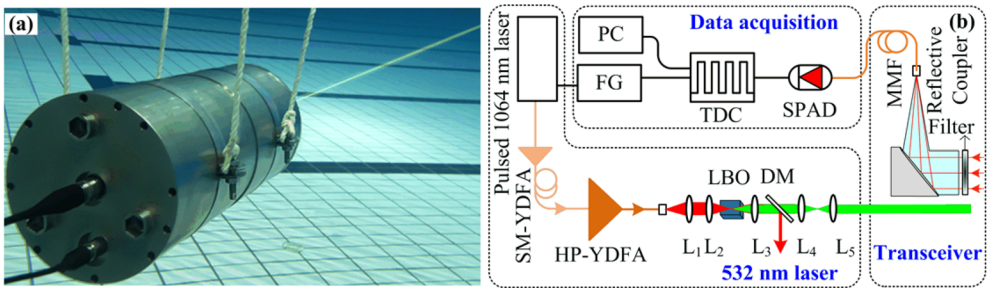

Fig. 1. (a) Photo of SPUL. (b) Optical layout of the SPUL. SM-YDFA: Single-Mode Ytterbium-Doped Fiber Amplifier; HP-YDFA: High-Power Ytterbium-Doped Fiber Amplifier; L: lens; LBO: lithium borate; MMF: Multimode fiber; SPAD: single-photon avalanche diode; TDC: time-to-digital converter; FG: function generator; PC: personal computer.

through water, the lidar can receive backscattered signal starting from the laser emission point. The geometric overlap factor, which represents the ratio of the laser beam that overlaps with the receiver FOV of the lidar, reaches 1 at a distance of ~ 1 m.

Photon detection is achieved using a compact silicon single-photon avalanche diode (SPAD) with an efficiency of approximately 52% and 100 dark counts per second (cps) at 532 nm. The electronic module utilizes a self-built function generator (FG) using a field programmable gate array (FPGA) to generate precise control signals for the laser and the high sample-rate TDC. The sample rate of the TDC is adjustable, with a maximum sampling rate of 10 ps. The photo of the SPUL completely submerged in water is shown in Fig. 1(a). The lidar chamber is made of Titanium alloy with high-pressure resistance characteristics so that the lidar can operate underwater up to 1 km. The capability of deploying the lidar system at this operating depth is verified by conducting pressurization tests up to 11 Megapascals (MPa), which corresponds to the pressure at a depth of over 1 km. This provides the possibility for lidar to be installed on underwater platforms, such as AUVs or ROVs, utilizing its capabilities to detect particles and dissolved matter for deep-sea water environmental surveys, as well as its high lateral resolution for high-resolution seafloor topography detection. The optical window of the lidar is made of sapphire, which can maintain >96% transmission under high pressure. The cylindrical lidar has a diameter of 20 cm and a length of 40 cm. The average power consumption of the lidar is ~ 80 W, and it weighs 15 kg. A summary of the key parameters of the lidar is presented in Table 1.

Table 1. Key parameters of the SPUL system

	Parameter	Value
Pulsed laser	Wavelength	532 nm
	Pulse duration	501 ps
	Pulse energy	100 nJ
	Pulse repetition rate	1 MHz
Telescope	Focal length	10.9 mm
	Mode-field diameter of the MMF	105 μm
SPAD	Detection efficiency at 532 nm	52%
	Dark count rate	100 cps
System	Size of the SPUL	Φ20 cm × 40 cm
	Power consumption	≈80 W
	Weight	15 kg

Optics EXPRESS

Oceanic lidars typically operate in the visible spectrum, where solar radiation is strong. This strong solar radiation during the day can be a major source of noise for oceanic lidars, especially single-photon based lidar. To suppress solar radiation noise, three designs were implemented in this work. Firstly, a narrow-band pulse laser with a linewidth of 0.04 nm was used in conjunction with a narrow-band filter to compress the received bandwidth and minimize the impact of solar radiation. Secondly, a collimator with a small aperture (4.8 mm) and narrow FOV (9.6 mrad) was used to reduce the solar radiation noise [33]. Finally, an underwater single-photon lidar was developed to take advantage of the water's absorption and scattering properties, which act as a natural filter to effectively suppress solar radiation. Additionally, operating underwater also eliminates potential interference caused by the air-sea interface during laser transmission.

3. Depth extraction algorithm and accuracy assessment

Single-photon lidars determine water depth by statistically analyzing the probability distribution of photons [29–31]. The temporal resolution of water depth (Δt) retrieved through statistical analyzing methods can be expressed as:

$$\Delta t = \sqrt{\tau_{TDC}^2 + \tau_{laser}^2 + \tau_{spad}^2 + \tau_{syn}^2}, \tag{1}$$

where τ_{TDC} is the temporal resolution of the TDC, τ_{laser} is the laser pulse duration (501 ps), τ_{spad} is the timing jitter of the SPAD (800 ps), τ_{syn} is the time jitter of the synchronous signal (10 ps).

The depth resolution of the entire lidar system was firstly evaluated in an experimental water tank at Xiamen University. During the experiment, a silver-white aluminum alloy disk with a diameter of 6 cm was placed at a depth of 0.8 m. The disk was fixed on a computer-controlled lifting platform with an elevation adjustment accuracy of 0.05 cm. The underwater lidar was positioned almost vertically to illuminate the disk, and the depth of the disk was adjusted by controlling the lifting platform. Data acquisition was performed with a TDC temporal resolution set to 10 ps, and the measurement results were represented by dots in Fig. 2(a). Due to the significantly stronger backscattered signals from the disk compared to the signals from the filtered tap water, the signals from the hard target were easily extracted, as shown in Fig. 2. To ensure measurement accuracy, the measurements were conducted after the water surface became calm. The time axis in the Fig. 2 has been transformed into depth in cm using a refractive index of 1.34. The FWHM of the backscattered histogram was ~ 1 ns, corresponding to a depth resolution of ~11 cm. This result agrees well with the calculated result (940 ps) obtained using Eq. (1).

To further enhance distance resolution, fitting algorithm is applied to process cumulative waveform obtained from single-photon measurements. As shown in Fig. 2(a), it is evident that the single-photon lidar can reconstruct waveform by using a high sampling-rate (10 ps) and accumulating data of 2 s. Initially, the photon-reconstructed waveform from the bottom is fitted using the following bi-Gaussian function:

$$y = \begin{cases} y_0 + H\exp[-0.5(x - x_c)^2/{w_1}^2] & (x<x_c) \\ y_0 + H\exp[-0.5(x - x_c)^2/{w_2}^2] & (x \geq x_c) \end{cases}, \tag{2}$$

where y_0 is the constant component, H is the amplitude, x_c is the position of bi-Gaussian peak, which is the bottom depth in this case, w_1 and w_2 are the half width, respectively, of the left and right part of the bi-Gaussian peak.

As shown in the Fig. 2(a), the measured data can be well fitted using Eq. (2), with a fitted R-squared value of 0.99. To validate the effectiveness of this algorithm, the underwater disk was subjected to two small vertical movements of 0.5 cm and 3.5 cm, respectively. As shown in the Fig. 2(a), the fitted peak shifts were found to be 0.6 cm and 3.6 cm, respectively, demonstrating that sub-cm depth resolution can be achieved by the algorithm. Although a higher sampling

Optics EXPRESS

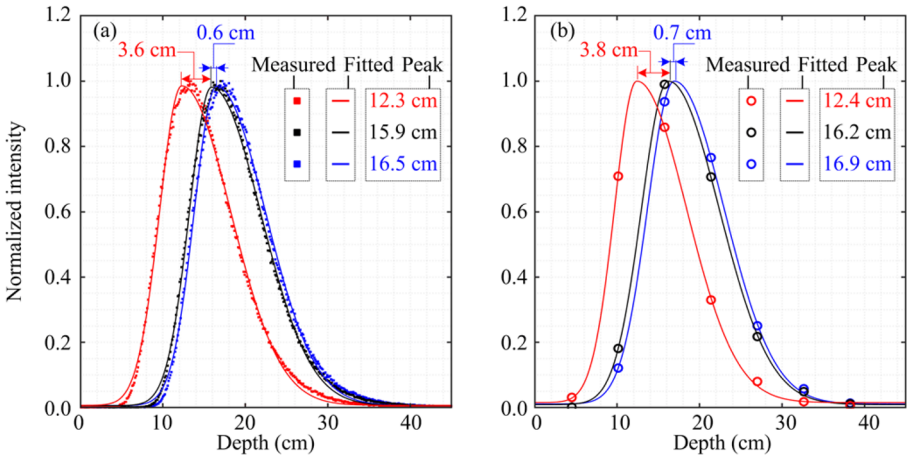

Fig. 2. Measurement results of the single-photon lidar for slight movements of a target in water with a sampling interval of (a) 10 ps (b) 500 ps. The rectangles in (a) and circles in (b) represent the measured points, while the lines indicate the results fitted by Eq. (2)

frequency is more favorable for waveform reconstruction, it poses challenges such as large data volume, difficulty in real-time data transmission and processing, and high costs on hardware. Therefore, a sampling interval of 500 ps was selected for field experiments. Additionally, although the sampling interval becomes sparser, the number of photons on a single bin increase. As shown in Fig. 2(b), with the same accumulation time of 2 s, using a sampling interval of 500 ps and a same fitting algorithm, a depth resolution of cm-level can still be achieved.

To validate the accuracy of the depth estimation based on the fitting algorithm at a sampling interval of 500 ps and its correlation with the backscattered signal intensity, a simulation was

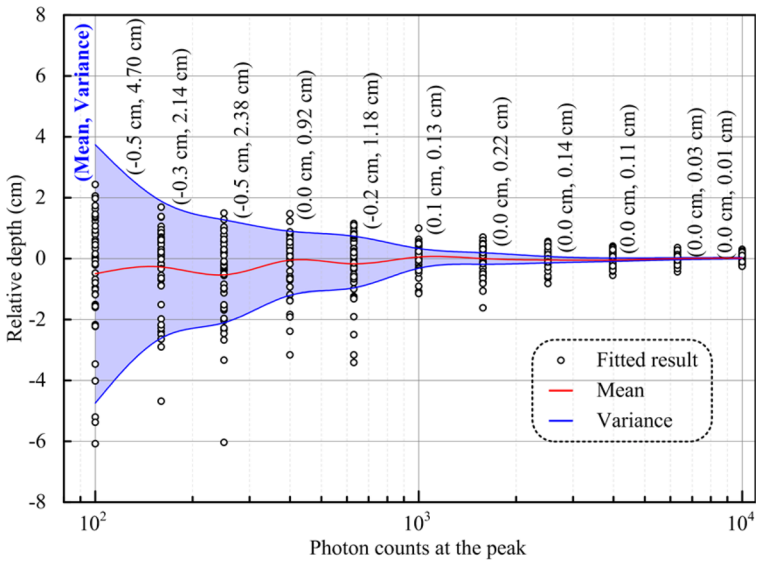

Fig. 3. Mean and variance of the central position obtained from fitting 50 sets of simulated data as the photon counts at the peak change from 10^2 to 10^4 with a sampling interval of 500 ps.

Optics EXPRESS

conducted. Specifically, a Poisson distribution was assumed for the photon count at each point in the waveform, and 50 independent photon-reconstructed waveforms were generated. Subsequently, the least squares fitting method was applied to each photon-reconstructed waveform using Eq. (2), and the mean and variance of the peak position obtained from the fitting were computed for each photon-reconstructed waveform. The results, as depicted in Fig. 3, show that the mean value of the peak position tends toward 0 cm as the photon count of the peak in echo waveform increases. Moreover, the variance decreases gradually with an increase in photon count. It is worth noting that the variance is less than 5 cm when the photon count at the peak position is 10^2, and less than 0.2 cm when the photon count is 10^3. These results suggest that the fitting algorithm outperforms the statistical method in terms of depth resolution.

4. Field experiments

4.1. Cruise survey

To validate the stability of the SPUL and the feasibility of our algorithms, field experiments were conducted on November 11, 2022, at Qinzhou Bay, Guangxi Province, China, with the ship track shown in Fig. 5(a), and on November 20, 2022, at Li'an Harbor, Hainan Province, China, with the ship track shown in Fig. 6(a). The underwater topographic maps in Fig. 5(a) and Fig. 6(a) are reconstructed based on sonar data. The water depth in the study area at both locations is less than 15 m. As shown in Fig. 4, the lidar was fixed in front of the ship, pointing downwards approaching vertically, and the laser outlet was positioned 0.3 m below the water surface. To validate the detection depth of the lidar, a sonar system was mounted on the same platform as the lidar, ensuring that they were detecting the same bottom. The sonar used in this study is a Biosonics DTX single-beam echosounder (SBES), which operates at 430 kHz with a narrow 3 dB beamwidth of 7.0°. The system has a pulse length of 0.1 ms, can measure distances ranging from 0.075 to 2,000 m. Additionally, the positions of the lidar and sonar relative to the water surface were calibrated prior to the experiment. Moreover, to minimize the influence of ship rolling and pitching on the measurements, the ship maintained a constant and smooth speed during the navigation process. The results from these experiments are shown in Fig. 5 and Fig. 6, respectively. The water in Qinzhou Bay is more turbid compared to that of Li'an Harbor.

Fig. 4. Picture of the shipborne single-photon underwater lidar during the field experiment.

Optics EXPRESS

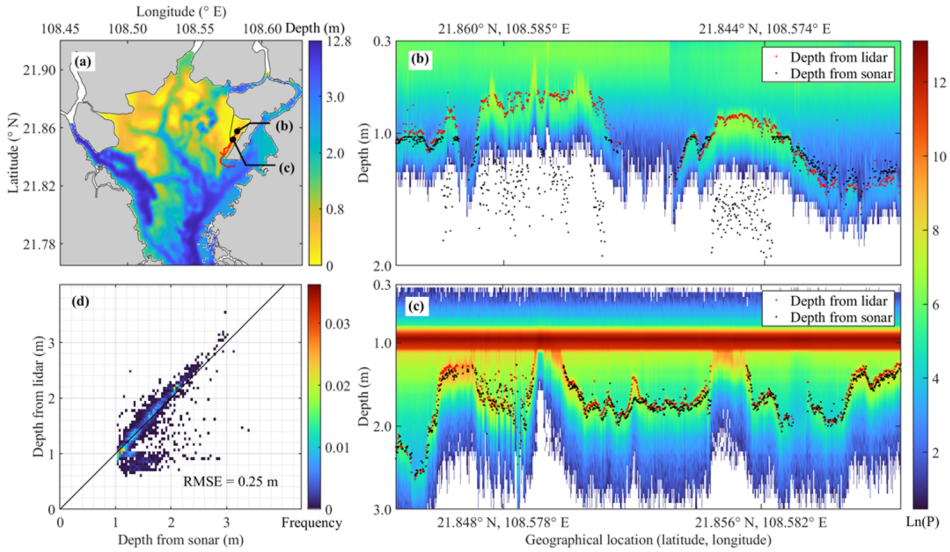

Fig. 5. Lidar cruise experiment at Qinzhou Bay. (a) Ship track (red solid line) and underwater topographic maps reconstructed using sonar data; (b) and (c) are time series of lidar observations at the two locations marked in (a), where Ln(P) represents the natural logarithm of the photon counts; (d) Consistency analysis between the lidar and sonar measurements.

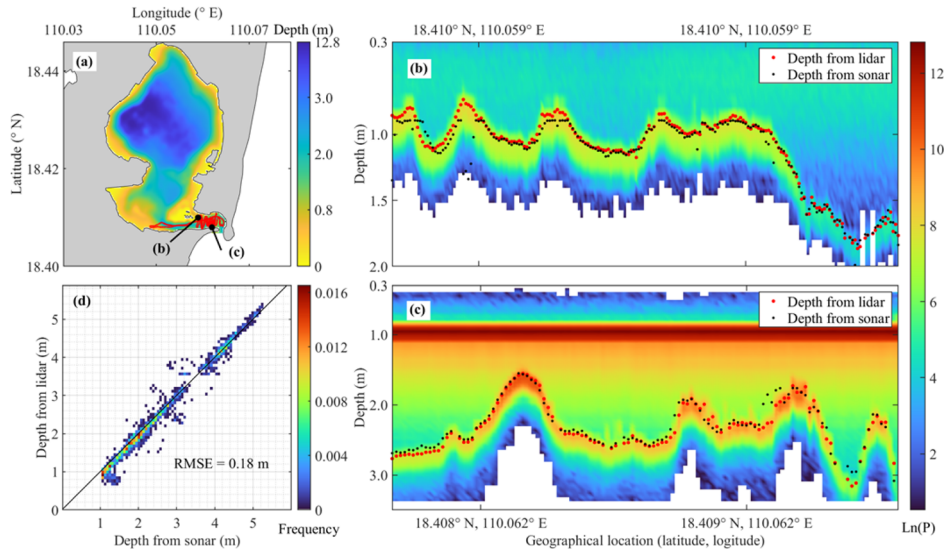

Fig. 6. Lidar cruise experiment at Li'an Harbor. (a) Ship track (red solid line) and underwater topographic maps reconstructed using sonar data; (b) and (c) are time series of lidar observations at the two locations marked in (a), where Ln(P) represents the natural logarithm of the photon counts; (d) Consistency analysis between the lidar and sonar measurements.

The measurement results are shown in Figs. 5 and 6, where the data considers the working depths of both instruments, and the sonar data have been quality-controlled to remove outliers. Figures 5(b), 5(c), 6(b), and 6(c) depict lidar-measured backscattered signals. During data

Optics EXPRESS

processing, photons at depth intervals of 5.6 cm within each 1-second interval are accumulated. Subsequently, the natural logarithm (Ln) of the accumulated photon counts (P) is calculated. Different colors are assigned to different Ln(P) values, producing the pseudo-color plots depicted in the figures. The red dots in Figs. 5(b) and (c), as well as Fig. 6(b) and (c), represent the depth measured by the lidar, where the water depth extraction algorithm used the fitting method presented in Section 3. The black dots in the figures represent the results measured by the sonar. Based on these two figures, the lidar measurements match well with the sonar results. It also highlights the prominent feature of the lidar compared to the sonar, which can not only detect signals from the bottom of the water for water depth inversion, but also detect backscattered signals from molecules and particles in the water, as indicated by the color scale in Fig. 5(b), 5(c), 6(b), and 6(c). The algorithm for extracting inherent optical properties (IOPs) of water based on the backscattered signal of particles is beyond the scope of this article and will be specifically addressed in future work.

In fact, the maximum single-pulse energy output of the laser can reach 1 uJ. However, during the two field experiments, the maximum pulse energy required was only 100 nJ. During these experiments, the laser pulse energy was toggled between 30 nJ and 100 nJ based on the intensity of the backscattered signal from the water. The pulse energy adjustment was manually performed during the experiments. As shown in Fig. 5(c) and Fig. 6(c), when the laser pulse energy is 100 nJ, a maximum value can be observed in the underwater backscattered signal at a depth of about 1 m below the water surface. This is due to the gradual increase of the geometric overlap factor, which reaches its maximum value of 1 at 1 m. However, in Fig. 5(b) and Fig. 6(b), when the laser pulse energy is 30 nJ, the strong signal from the bottom overwhelms the signal from the water, including the peak signal at 1 m. It is worth noting that, despite this, the bottom signal is still kept below the saturation count rate of the single-photon detector (40 MHz), with the average number of photons in one distance bin is less than 0.01, thus avoiding the introduction of range walk error (RWE) [34]. When the pulse energy was set to 100 nJ, if the peak of the echo signal from the bottom of the water was ~ 1 m, extracting the peak value becomes challenging. In such cases, a geometric correction factor needs to be applied to the backscattered signal beforehand.

The consistency analysis of depth data obtained from the lidar and sonar measurements is presented in Fig. 5(d) and Fig. 6(d), respectively. There are still some differences between the results due to the fact that the sonar has a larger beam angle (7°) compared to the lidar (0.55°), resulting in a broader coverage area for the sonar. Nevertheless, the measurements obtained from the two different instruments demonstrate a high level of consistency in both Qinzhou Bay and Li'an Harbor, with RMSE of 0.25 m and 0.18 m, respectively. This verifies the effectiveness and robustness of the SPUL system and the bathymetric extraction algorithm.

4.2. Stationary observation lasting 24 hours

To verify the continuous day and night observation capability of the SPUL, a stationary observation was conducted at Li'an Harbor lasting 24 hours. The weather conditions during the observation were clear and sunny, with no clouds. Throughout the experiment, the ship equipped with the lidar system remained anchored in water with an approximate depth of 5 m.

In Fig. 7, the vertical profile of the lidar data is depicted. The black dots represent the inverted water depth data obtained by the lidar, while the red line represents the water depth derived from tidal data, which was acquired from the national marine data center and adjusted for the vertical distance between the tidal datum plane and the seabed at the observation station. By selecting several typical lidar backscattered signals at different times, as shown in Fig. 8, it can be seen that during nighttime, as shown in Fig. 8(a), the single-photon lidar exhibits low noise and does not require denoising processing. However, during daytime, as shown in Fig. 8(b), although the single-photon lidar has significantly suppressed the noise, some noise still enters the detector, especially at noon when solar radiation is the strongest, resulting in a hundredfold increase in

Optics EXPRESS

noise compared to the night. Nevertheless, accurate depth information can still be extracted by removing the noise and using the fitting algorithm. Note that the peak observed at a depth of 1 m in Fig. 7 is attributed to the gradual increase of the geometric overlap factor, which reaches its maximum value of 1 at this depth, as clearly depicted in Fig. 8.

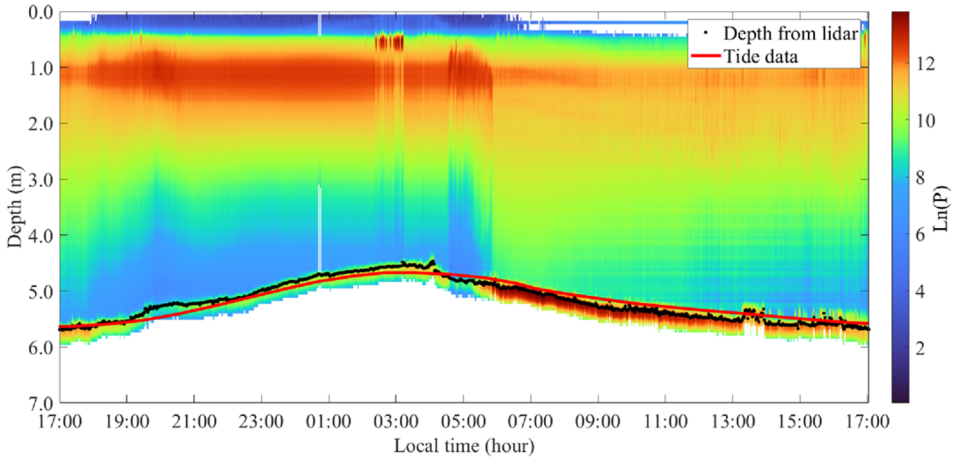

Fig. 7. Lidar stationary observation at Li'an Harbor for continuous 24 hours.

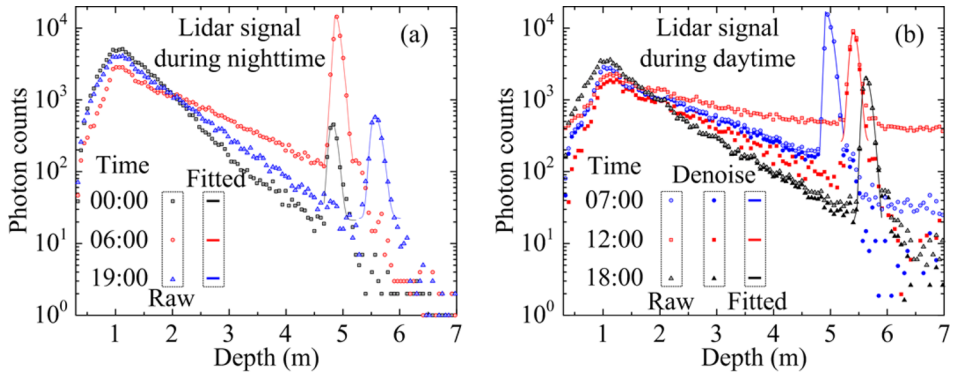

Fig. 8. Typical lidar backscattered signals during nighttime (a) and daytime (b). Hollow symbols, including circles, rectangles, and triangles, represent the raw lidar signals, while solid symbols, including circles, rectangles, and triangles, represent the lidar signals after subtracting background noise. The line represents the result of fitting the bottom signal using Eq. (2).

Based on the results of the 24-hour observation, the water depth measured by the lidar exhibited consistency with the water depth derived from tidal data, confirming the continuous day and night observation capability and stability of the SPUL. It is worth noting that, due to being limited by the shallow water depths in these two bays, the single-photon bathymetric lidar can only detect water depths within 6 m. Furthermore, in our previous experiments, the single-photon lidar has been validated to detect distances up to 105 m and has a maximum detection depth of approximately $5.5/K_d$, where K_d represents the diffuse attenuation coefficient [17]. In the future, additional experiments will be conducted to further verify its bathymetric capabilities.

Optics EXPRESS

5. Conclusion

In this work, a single-photon underwater lidar was proposed and demonstrated for continuous day and night measurement of shallow-water depth, addressing a challenge faced by single-photon lidars due to interference from solar background radiation. Fortunately, submerging the lidar underwater eliminates interference from the air-water interface. Moreover, water acts as a natural filter, absorbing and scattering solar radiation, thereby greatly reducing background noise from solar background radiation.

Regarding the hardware design, a highly sensitive single-photon detection technique was employed in this system, enabling the integration of the lidar into a water-tight and pressure-resistant compartment. This technique allows for the detection of shallow water depth with a 100 nJ pulse energy and a 4.8 mm aperture telescope. To enable daytime operation, a small-aperture optical telescope was designed and narrowband filter technology was employed. Ultimately, the lidar was integrated into a compact aluminum alloy cylindrical chamber with a diameter of 20 cm and a length of 40 cm, with a power consumption of $\sim$ 80 W. The system is capable of operating underwater up to a depth of 1 km.

Regarding the depth extraction algorithm, a method based on a bi-Gaussian model and least squares fitting was proposed to extract water depth, resulting in a significant improvement in the depth resolution of the single-photon lidar. Numerical simulations demonstrate that, with a peak photon count of 1000 and a sampling-rate of 500 ps, the variance of the extracted depth is less than 1 cm. Additionally, the photon-reconstructed waveform has the potential to be used for inversion of the bottom substrate type, which is an important motivation for developing fitting algorithms.

In future work, a large number of comparative experiments will be conducted to further validate the robustness of our SPUL. Furthermore, other techniques for suppressing solar radiation noise will be incorporated, such as utilizing laser wavelengths that align with Fraunhofer lines. Although data fitting methods are more time-consuming compared to statistical analysis methods, optimization algorithms and hardware upgrades will be employed to improve processing speed. Moreover, we plan to develop an inversion algorithm for water column IOPs, enabling simultaneous inversion of the depth and IOPs. Currently, the challenge in inverting IOPs arises from the near-field signal being affected by the geometric overlap factor. Additionally, we intend to utilize fitted histogram data for remote sensing of the bottom substrate type, including coral and seagrass, similar to the approach employed in full waveform bathymetric lidars. Lastly, integrating this single-photon lidar into underwater platforms such as AUVs and using it in conjunction with sonar is expected to not only enable obstacle avoidance for underwater platforms but also facilitate high-precision depth information extraction in deep-sea environments, including for small targets like fish and shrimp. In summary, we believe that this work holds significant potential for practical applications, whether by integrating the lidar into AUVs or shipborne platforms, thereby enhancing our ability to obtain oceanic information.

Funding. National Key Research and Development Program of China (2022YFB3901704); Blue Carbon Ecosystem Assessment, Restoration and Accounting: A Tencent supported project; Innovation Program for Quantum Science and Technology (2021ZD0303102); Joint Funds of the National Natural Science Foundation of China (U2106210); Natural Science Foundation of Fujian Province (2020J01026); Fujian Provincial Central Guided Local Science and Technology Development Special Project (2022L3078); MEL-RLAB Joint Fund for Marine Science & Technology Innovation..

Disclosures. The authors declare no conflicts of interest.

Data availability. The data that support the findings of this study are available from the corresponding author upon reasonable request.

References

1. C.-K. Wang and W. D. Philpot, "Using airborne bathymetric lidar to detect bottom type variation in shallow waters," Remote Sens. Environ. **106**(1), 123–135 (2007).

Optics EXPRESS

2. V. Klemas, "Beach profiling and LIDAR bathymetry: An overview with case studies," J. Coastal Res. **277**, 1019–1028 (2011).
3. G. Mandlburger, H. Lehner, and N. Pfeifer, "A comparison of single photon and full waveform lidar," ISPRS Ann. Photogrammetry, Remote Sens. Spatial Inform. Sci. **4**, 397–404 (2019).
4. G. Mandlburger, M. Pfennigbauer, and N. Pfeifer, "Analyzing near water surface penetration in laser bathymetry—A case study at the River Pielach," ISPRS Ann. Photogrammetry, Remote Sens. Spatial Inform. Sci. **5**, W2 (2013).
5. C. Wang, Q. Li, Y. Liu, *et al.*, "A comparison of waveform processing algorithms for single-wavelength LiDAR bathymetry," ISPRS J. Photogrammetry, Remote Sens. **101**, 22–35 (2015).
6. H. H. Kim, P. O. Cervenka, and C. B. Lankford, *Development of an Airborne Laser Bathymeter* (National Aeronautics and Space Administration, 1975).
7. P. J. Kinzel, C. J. Legleiter, and J. M. Nelson, "Mapping river bathymetry with a small footprint green LiDAR: applications and challenges 1," J. American Water Resour Assoc. **49**(1), 183–204 (2013).
8. D. Su, F. Yang, Y. Ma, *et al.*, "Classification of coral reefs in the South China Sea by combining airborne LiDAR bathymetry bottom waveforms and bathymetric features," IEEE Trans. on Geosci. Remote Sens. **57**(2), 815–828 (2019).
9. M. Wang, Z. Wu, F. Yang, *et al.*, "Multifeature extraction and seafloor classification combining LiDAR and MBES data around Yuanzhi Island in the South China Sea," Sensors **18**(11), 3828 (2018).
10. L. Janowski, R. Wroblewski, M. Rucinska, *et al.*, "Automatic classification and mapping of the seabed using airborne LiDAR bathymetry," Engineering Geology **301**, 106615 (2022).
11. H. M. Tulldahl, P. Philipson, H. Kautsky, *et al.*, "Sea floor classification with satellite data and airborne lidar bathymetry," in *Ocean Sensing and Monitoring V* (SPIE, 2013), 100–115.
12. G. Mandlburger, M. Pfennigbauer, R. Schwarz, *et al.*, "Concept and performance evaluation of a novel UAV-borne topo-bathymetric LiDAR sensor," Remote Sens. **12**(6), 986 (2020).
13. S. E. Mitchell and J. P. Thayer, "Ranging through shallow semitransparent media with polarization lidar," J. Atmos. Oceanic Technol. **31**(3), 681–697 (2014).
14. D. Ventura, "Coastal zone mapping with the world's first airborne multibeam bathymetric lidar mapping system" (2020).
15. M. Shangguan, H. Xia, C. Wang, *et al.*, "Dual-frequency Doppler lidar for wind detection with a superconducting nanowire single-photon detector," Opt. Lett. **42**(18), 3541–3544 (2017).
16. M. Shangguan, H. Xia, C. Wang, *et al.*, "All-fiber upconversion high spectral resolution wind lidar using a Fabry-Perot interferometer," Opt. Express **24**(17), 19322–19336 (2016).
17. M. Shangguan, Z. Yang, Z. Lin, *et al.*, "Compact long-range single-photon underwater lidar with high spatial-temporal resolution," IEEE Geosci. Remote Sens. Lett. **20**, 1–5 (2023).
18. M. Shangguan, Z. Yang, M. Shangguan, *et al.*, "Remote sensing oil in water with an all-fiber underwater single-photon Raman lidar," Appl. Opt. **62**(19), 5301–5305 (2023).
19. M. Shangguan, Z. Liao, Y. Guo, *et al.*, "Sensing the profile of particulate beam attenuation coefficient through a single-photon oceanic Raman lidar," Opt. Express **31**(16), 25398–25414 (2023).
20. M. Shangguan, Y. Guo, Z. Liao, *et al.*, "Sensing profiles of the volume scattering function at 180° using a single-photon oceanic fluorescence lidar," Opt. Express **31**(24), 40393–40410 (2023).
21. C. E. Parrish, L. A. Magruder, A. L. Neuenschwander, *et al.*, "Validation of ICESat-2 ATLAS bathymetry and analysis of ATLAS's bathymetric mapping performance," Remote Sens. **11**(14), 1634 (2019).
22. L. A. Magruder, J. Markel, and C. Simurda, "An overview of ICESat-2 bathymetric capabilities and discoveries," Proc. SPIE **12110**, 1211009 (2022).
23. K. Y. Shrestha, W. E. Carter, K. C. Slatton, *et al.*, "Shallow bathymetric mapping via multistop single photoelectron sensitivity laser ranging," IEEE Trans. on Geosci. Remote Sens. **50**(11), 4771–4790 (2012).
24. R. Brown, P. Hartzell, and C. Glennie, "Evaluation of SPL100 single photon lidar data," Remote Sens. **12**(4), 722 (2020).
25. X. Chen, W. Kong, T. Chen, *et al.*, "High-repetition-rate, sub-nanosecond and narrow-bandwidth fiber-laser-pumped green laser for photon-counting shallow-water bathymetric Lidar," Results Phys. **19**, 103563 (2020).
26. J. J. Degnan, "Scanning, multibeam, single photon lidars for rapid, large scale, high resolution, topographic and bathymetric mapping," Remote Sens. **8**(11), 958 (2016).
27. X. Shen, W. Kong, P. Chen, *et al.*, "A shipborne photon-counting lidar for depth-resolved ocean observation," Remote Sens. **14**(14), 3351 (2022).
28. D. McLeod, J. Jacobson, M. Hardy, *et al.*, "Autonomous inspection using an underwater 3D LiDAR," in *OCEANS-San Diego* (IEEE, 2013), 1–8.
29. U. C. Herzfeld, B. W. McDonald, B. F. Wallin, *et al.*, "Algorithm for detection of ground and canopy cover in micropulse photon-counting lidar altimeter data in preparation for the ICESat-2 mission," IEEE Trans. on Geosci. Remote Sens. **52**(4), 2109–2125 (2014).
30. J. Zhang and J. Kerekes, "An adaptive density-based model for extracting surface returns from photon-counting laser altimeter data," IEEE Geosci. Remote Sens. Lett. **12**(4), 726–730 (2015).
31. R. Ma, W. Kong, T. Chen, *et al.*, "KNN Based Denoising Algorithm for Photon-Counting LiDAR: Numerical Simulation and Parameter Optimization Design," Remote Sens. **14**(24), 6236 (2022).

Optics EXPRESS

32. J. H. Churnside and J. A. Shaw, "Lidar remote sensing of the aquatic environment: invited," Appl. Opt. **59**(10), C92–C99 (2020).
33. J. J. Degnan, "Photon-counting multikilohertz microlaser altimeters for airborne and spaceborne topographic measurements," J. Geodynamics **34**(3-4), 503–549 (2002).
34. Y. Ma, S. Li, W. Zhang, *et al.*, "Theoretical ranging performance model and range walk error correction for photon-counting lidars with multiple detectors," Opt. Express **26**(12), 15924–15934 (2018).